Reversible patterning of spherical shells through constrained buckling

J. Marthelot,[1] P.-T. Brun,[2] F. López Jiménez,[1] and P. M. Reis[1,3,*]

[1]*Department of Civil Engineering, Massachusetts Institute of Technology, Cambridge, Massachusetts 02139, USA*

[2]*Department of Mathematics, Massachusetts Institute of Technology, Cambridge, Massachusetts 02139, USA*

[3]*Department of Mechanical Engineering, Massachusetts Institute of Technology, 77 Massachusetts Avenue,
Cambridge, Massachusetts 02139, USA*

Recent advances in active soft structures envision the large deformations resulting from mechanical instabilities as routes for functional shape morphing. Numerous such examples exist for filamentary and plate systems. However, examples with double-curved shells are rarer, with progress hampered by challenges in fabrication and the complexities involved in analyzing their underlying geometrical nonlinearities. We show that on-demand patterning of hemispherical shells can be achieved through constrained buckling. Their postbuckling response is stabilized by an inner rigid mandrel. Through a combination of experiments, simulations, and scaling analyses, our investigation focuses on the nucleation and evolution of the buckling patterns into a reticulated network of sharp ridges. The geometry of the system, namely, the shell radius and the gap between the shell and the mandrel, is found to be the primary ingredient to set the surface morphology. This prominence of geometry suggests a robust, scalable, and tunable mechanism for reversible shape morphing of elastic shells.

I. INTRODUCTION

Active soft structures are burgeoning in engineering for their promise of compliant, dynamic, and programmable mechanisms. Examples include soft robotics [1,2], deployable structures [3–5], surface patterning [6,7], and four-dimensional printing [8]. Mechanical instabilities have been central to harnessing these new modes of shape morphing that derive from the ensuing large elastic deformations [9]. As such, shape morphing has been widely studied in slender filamentary structures [10] and plates [6,11]. By contrast, instances of surface patterning of curved shells are yet to be fully exploited in technology, even if examples do exist in nature (e.g., pollen grains [12] and drying green peas [7]), and synthetic analog systems have been developed at the colloidal scale [13]. This discrepancy is surprising given the ubiquitousness of shells for enclosure, protection, and load bearing; from capsids [14] and colloidosomes [15] to metallic shells [16] and architectural domes [17].

Here, we study the postbuckling patterns obtained by pneumatic actuation of a thin elastic shell that is constrained from within by a rigid mandrel [Fig. 1(a)]. The patterns comprise a periodic lattice of dimples that tile the originally spherical shell as they are sequentially triggered through buckling. Once fully developed, the resulting pattern morphs into a reticulated network of sharp ridges that separate adjacent facets of the tiling [Fig. 1(a4)]. Combining experiments, scaling analyses, and computer simulations, we rationalize the mechanics of this system. Starting with the dimple as an individual building block, we characterize how its size depends on the radius of the shell and the gap between the shell and the mandrel. A geometric construction is introduced to describe the nucleation process. Once the pattern is fully developed, in the regime of sharp ridges, we reduce the local deformation of the shell to a two-dimensional problem and describe the evolution of the ridge profile for increased loading. Our minimal theoretical framework allows us to customize and control the surface

patterning toward programmable topography. This versatility in tuning the morphology of the patterns is in sharp contrast with classic pattern formation of bilayer systems [18–21], where patterns are primarily mediated by elasticity and set by the material parameters that cannot be readily changed.

II. PERIODIC SURFACE PATTERNING THROUGH BUCKLING

In our experiments, we used elastomeric hemispherical shells produced via rapid fabrication techniques [22], with radii in the range $25 \leqslant R$ [mm] $\leqslant 77.5$. A rigid hemispherical foundation of radius $R_m < R$ was placed concentrically inside the shell, such that the gap between the shell centerline and the surface of the outer mandrel was $G = R - R_m$ [Fig. 1(b)]. The ensemble was mounted onto a base plate, and sealed, to pneumatically control the volume within the gap, while monitoring the pressure. In Fig. 1(a) and Movie S1 [23], we present a series of representative photographs of the obtained buckling patterns for a shell ($R = 38.5$ mm, $h = 200$ μm, $G = 2$ mm, VPS-32) as its volume is progressively decreased [(a1)–(a4) $\Delta V = \{0,8,15,30\}$ ml, respectively]. These patterns comprise a periodic tiling of dimples, which are inwardly inverted localized caps of the hemispherical shell. When the volume enclosed under the shell is decreased, these dimples appear progressively and are stabilized by contact with the mandrel. The regions in between neighboring dimples then become increasingly sharper [Fig. 1(a3)] and morph into a network of sharp ridges [Fig. 1(a4)]. The pattern topography is quantified by digitizing the surface using a three-dimensional laser scanner, to determine the centroids of each dimple.

The dimple size, L, is defined as the distance between two neighboring centroids, averaged over the entire pattern. Each dimple grows until it comes into contact with the mandrel. Following the geometrical argument of Pogorelov [24,25], by assuming that an inverted cap of radius R grazes the mandrel, yields the characteristic length

$$\ell_g = 2\sqrt{RG}, \qquad (1)$$

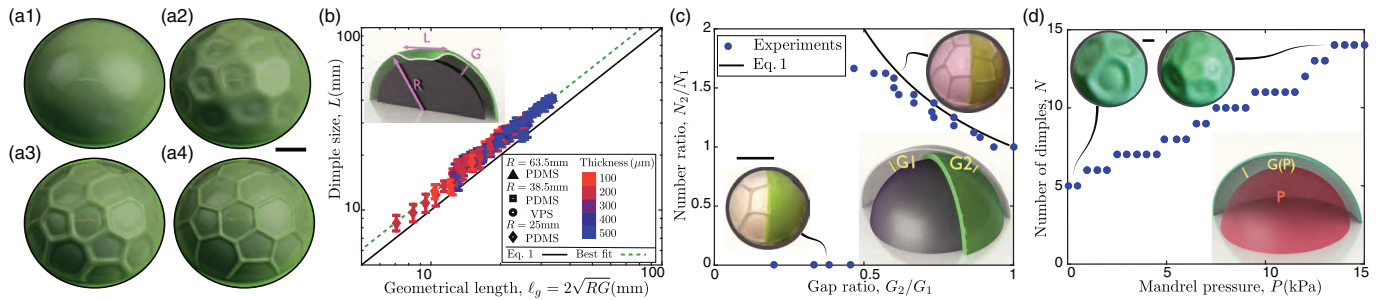
*Corresponding author: preis@mit.edu

FIG. 1. (a) Photographs of a shell as its volume is progressively decreased. (b) The dimple size L scales linearly with the characteristic length $\ell_g = 2\sqrt{RG}$. Solid black (respectively, green dashed) line represents the geometric prediction (respectively, the best fit of the data). (c) Ratio of the numbers of dimples N_2/N_1 vs the gap ratio G_2/G_1. The solid line is the prediction from Eq. (1). (d) Number of dimples N versus the pressure P in the inner inflatable mandrel. Scale bars indicate 20 mm.

which we use to model the diameter of each dimple when it first contacts the mandrel. In Fig. 1(b), we plot L as a function of the characteristic length ℓ_g, for shells with different stiffnesses $E = \{1.25, 1.96\}$ MPa, thicknesses $140 \leqslant h \ [\mu m] \leqslant 520$, radii $R = \{25, 38.5, 63.5\}$ mm, and gaps $0.4 \leqslant G \ [mm] \leqslant 4.2$. The data collapse onto a linear master curve. We find that the best fit of the data [dashed line in Fig. 1(b)] is obtained for $L/\ell_g = 1.22 \pm 0.05$, so that L is independent of the material properties and thickness of the shell over the experimental conditions explored. These results contrast with the characteristic buckling length near threshold predicted by the classic theory for pressurized shells [16,26,27], $\ell_b = 2\pi\sqrt{Rh}/[12(1-\nu^2)]^{1/4}$, for a spherical shell with radius R, thickness h, and Poisson's ratio ν. Note that the classical bifurcation mode is only valid for a small range of deflection, of the order of the shell thickness, whereupon the buckling mode localizes at the pole as an inward dimple [28]. In our constrained case, the selection of the dimple size occurs well into the postbuckling regime and the geometry of the gap dictates the sequence of buckling events. For gaps smaller than the shell thickness, the shell can fully conform to the mandrel, with no dimples, as the deformation is smoothly accommodated through stretching. At the opposite end, in the limit of large gaps, the first dimple may display localized features (s cones) [29,30], prior to triggering a second dimple. To further illustrate the key role of geometry in this problem we proceed to vary the gap G in two ways: spatially and dynamically.

In Fig. 1(c), we present snapshots for the case where G is a step function; the radius of the mandrel decreases sharply along one of its great circles, from G_1 (left region) to G_2 (right region), with $G_1 > G_2$. We find that there are two possible outcomes: (i) two populations with different dimple sizes coexist on the shell, separated by a common ridge at the locus of the step; and (ii) for small enough values of G_2, only one half of the shell (with G_1) is dimpled, whereas the shell conforms uniformly to the mandrel on the other half. These two regimes are evident from Fig. 1(c), where we plot the ratio between the number of dimples N_1 and N_2 in the regions with G_1 and G_2, respectively, as a function of G_1/G_2 for a VPS-32 shell ($R = 63.5$ mm, $h = 320 \ \mu m$, $0.4 < G \ [mm] < 4.2$). From Eq. (1), we expect $N_1/N_2 = G_2/G_1$ [Fig. 1(c), solid curve], which is in agreement with the experimental data, except for case (ii) with $N_2 = 0$, when G_2 becomes of the

order of the shell thickness and the shell conforms to the mandrel. Therefore, modulation of the gap between the shell and the mandrel can be an effective route to produce Janus-like particles [31,32], with regions of distinct surface topography.

We now demonstrate that the pattern size may also be tuned dynamically when actively controlling the gap between the shell and the mandrel. We used an inflatable elastic mandrel (Young's modulus $E_m = 1.25$ MPa, thickness $h_m = 2.2$ mm), whose size can be modulated by actuating its internal pressure, P. This inner pressure is set independently from the pressure inside the gap. Reverting to an unbuckled configuration each time P is changed, we find that N varies in discrete steps [Fig. 1(d)]. To rationalize our observations we return to the rigid mandrel case and proceed to investigate the pattern formation. First, we focus on the nucleation of the dimples at moderate pressures of the order of the critical buckling pressure. Second, we describe how the fully developed periodic pattern morphs into a network of sharp ridges for larger values of depressurization.

III. NUCLEATION OF THE PERIODIC BUCKLING PATTERN

In Figs. 2(a1)–2(a6), we present a sequence of photographs of a vinylpolysiloxane (VPS) shell ($R = 38.5$ mm, $h = 430 \ \mu m$, $G = 3.05$ mm) that is progressively depressurized, from the onset of the first dimple up to full coverage of the surface ($\Delta V = \{1.05, 2.26, 3.03, 4.17, 5.22, \text{ and } 15\}$ mL, respectively). A single dimple first appears at $\mathbf{d}_1$, the locus of the largest imperfection [26] set uncontrollably by the fabrication process [Fig. 2(a1)]. This dimple then itself acts as a seed for the second buckling event nucleated at $\mathbf{d}_2$, at a distance L from $\mathbf{d}_1$ [permissible at any point of the circle of center $\mathbf{d}_1$ and radius L plotted in Fig. 2(a2)]. Both dimples now act as a combined seed and the third dimple forms where the perturbation is strongest; the intersection of the two circles of radius L centered at $\mathbf{d}_1$ and $\mathbf{d}_2$, respectively [Fig. 2(a3)]. The subsequent dimples are induced following an identical inductive scheme [Figs. 2(a4) and 2(a5)] until the entire surface of the hemisphere is populated. By design, this geometrical construction leads to a hexagonal tiling and the corresponding Voronoi mesh of the centers of the dimples overlaps with ridges of the pattern [Fig. 2(a6)]. However, since a curved surface is not compatible with a perfect hexagonal lattice [33–35], the
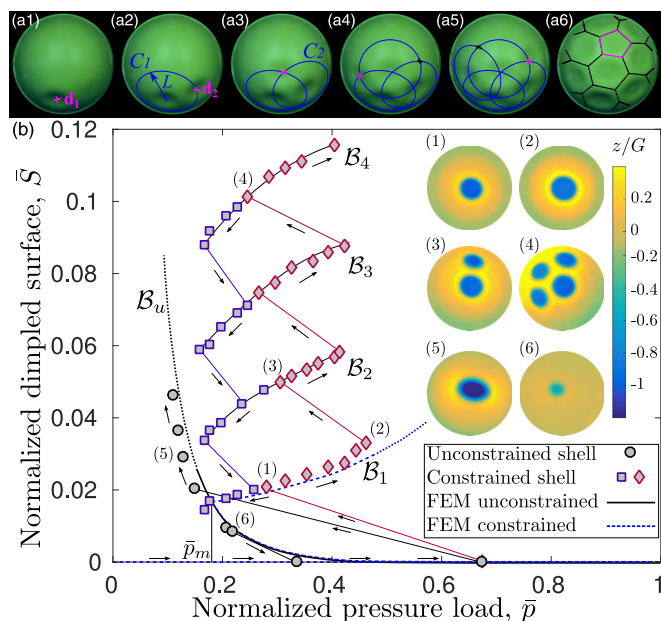
FIG. 2. (a1)–(a6) Progression of the dimple front as the volume is decreased. The dimple centered at $\mathbf{d_2}$ may form anywhere on the circle C_1 of center $\mathbf{d_1}$ and radius L. C_1 and C_2 (centered on d_2 with radius L) determines the locus of the next dimple, thereby extending the pattern, which eventually forms a regular hexagonal tiling on the sphere (with some distributed defects). (b) Bifurcation diagram. The buckled area $\bar{S} = S/2\pi R^2$ is shown as a function of the normalized pressure $\bar{p} = \Delta p/p_{\text{ct}}$. Experimental data for the unconstrained (circles) and constrained shell (diamonds/squares for increasing/decreasing ΔV). FEM results show unconstrained (solid line) and constrained (dashed lines) cases; regions where the corresponding experimental configuration is nonaxisymmetric are indicated by the dotted line (axisymmetry is assumed in the numerics). Inset: Surface topography z/G of the shell for the constrained case (1)–(4) and the unconstrained case (5) and (6).

patterns contain pentagonal topological defects of the lattice [Fig. 2(a6)]. For a given shell, the buckling process is highly reproducible, even if the order in which the dimples appear and their positions can be tailored and controlled by seeding defects at specific locations on the surface of the specimen [23].

The resulting postbuckling periodic pattern is now contrasted to the *unconstrained* case (no mandrel) for the same shell. Specifically, we compare the dimensionless cumulative surface area covered by the dimples $\bar{S} = S/2\pi R^2$ in both cases (i.e., the area S of the regions that are inverted normalized by the total area of the hemisphere of radius R). The digitized surface profile of the sample [Fig. 2(b), inset] is used to evaluate $\bar{S}$. To quantify the extent of loading, we define $\bar{p} = \Delta p/p_{\text{ct}}$, where Δp is the pressure differential between the inside of the shell and the outer ambient pressure, and p_{ct} is the classic critical buckling pressure prediction [26], $p_{\text{ct}} = 2E/\sqrt{3(1-\nu^2)}(h/R)^2$.

In Fig. 2(b), we plot $\bar{S}$ versus $\bar{p}$, for both the unconstrained and the constrained cases ($R = 38.5$ mm, $h = 240 \ \mu$m, $G = 2.2$ mm). The onset of the first dimple (in both cases) occurs at $\bar{p} = 0.67$, since intrinsic imperfections of the shells reduce the buckling pressure to a fraction of the critical pressure

required for a perfect shell to buckle, p_{ct} [26,36–38]. After a dimple appears in the unconstrained case [circles in Fig. 2(b) and insets (5) and (6)], its size increases throughout the process, $\bar{p}$ decreases monotonically [39], and no other dimples are observed. Conversely, in the constrained case [Fig. 2(b), diamonds for increasing $\bar{p}$ and squares for decreasing $\bar{p}$], a single large buckled region cannot occur since the shell eventually contacts the inner rigid mandrel at the pressure $\bar{p}_m$. As a result of this geometrical frustration, an increase in $\bar{S}$ comes at the expense of an increase in $\bar{p}$. Increasing $\bar{p}$ along the branch $\mathcal{B}_1$, we find that a second dimple eventually appears for $\bar{p} \simeq 0.5$ and the system jumps to a new branch $\mathcal{B}_2$. A similar sequence of events yields subsequent dimples until the pattern is fully developed. The associated jumps onto new branches ($\mathcal{B}_3$ denotes the third dimple and $\mathcal{B}_4$ for the fourth) are reported in Fig. 2(b). The threshold pressure from one branch to the next occurs at an approximately constant value of $\bar{p} \simeq 0.5$ for all dimples. The reverse path, decreasing $\bar{p}$ from the fully developed pattern down to the unbuckled configuration, is presented in Fig. 2(b) (squares). Each branch is followed down until a dimple snaps back and the system jumps to a lower branch, with strong hysteresis. The various jumps from one branch to another (as dimples disappear sequentially) occur at a similar value of pressure, $\bar{p} \simeq 0.2$.

To further explore the role of the mandrel in our system, we performed numerical simulations using a finite element method (FEM) accounting for contact between the shell and mandrel [23]. The FEM results [dashed and solid lines in Fig. 2(b) for the constrained and unconstrained cases, respectively] are superposed onto the experimental data with favorable agreement. For the values of $\bar{p}$ beyond which the experimental configuration is nonaxisymmetric (not considered in the simulations), the FEM data are plotted as dotted lines. We recover the fact that $\bar{p}$ increases (respectively, decreases) with $\bar{S}$ in the constrained (respectively, unconstrained) case. These results suggest that the modified energetics induced by the constraining mandrel [23] are at the basis of the periodic buckling patterns.

IV. FROM DIMPLES TO A RETICULATED PATTERN OF SHARP RIDGES

Thus far, we have identified the role of geometry in the selection of the dimples size and number, as well as their sequential apparition at the surface of the shell. Next, we turn to examining the patterns obtained in the limit of large depressurization, i.e., beyond the point of full coverage [Figs. 1(a2)–1(a4)]. As $\bar{p}$ is increased, the ridges between neighboring dimples become increasingly sharper, and eventually localize into a reticulated network [Fig. 1(a4)]. We have cycled the pressure ~ 1000 times in the range $0 \leqslant \bar{p} \leqslant 30$ and found that the process is fully reversible, with no structural damage, owing to the elastomeric nature of the shells.

We now quantify the morphology of the ridges and measure their width, λ, and amplitude, δ, using a laser sheet [Fig. 3(a), inset]. In Fig. 3(a), we show an example of the height profile of a single ridge for a shell ($R = 38.5$ mm, $h = 450 \ \mu$m, $G = 2.2$ mm) at $\Delta p = 510$ Pa (black dotted line). The corresponding dependencies of λ and δ on Δp are plotted
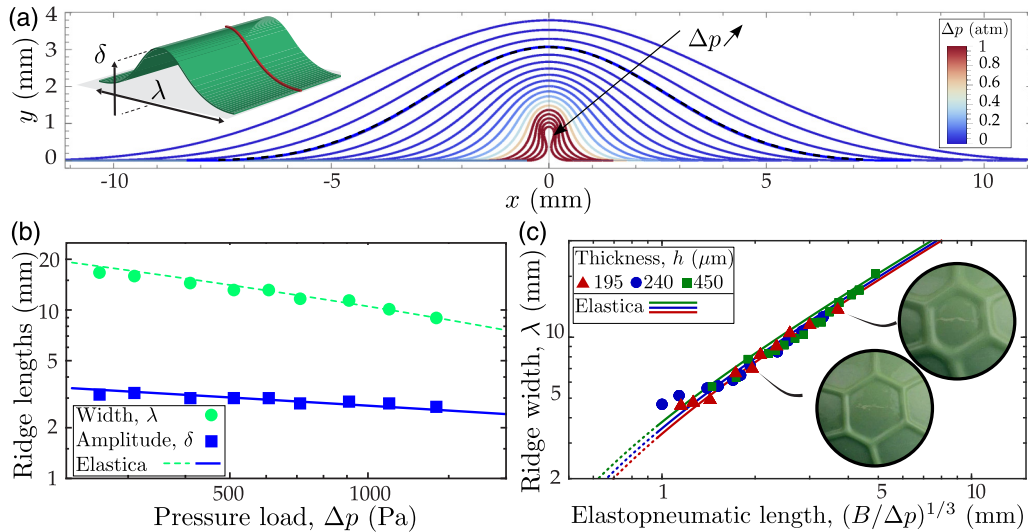
FIG. 3. (a) Evolution of the computed ridge profile predicted by integration of the *elastica*, for increasing values of Δp. The dotted line corresponds to an experimental profile for a polydimethylsiloxane (PDMS) shell ($R = 38.5$ mm, $h = 450\ \mu$m, $G = 2.2$ mm, $\Delta p = 510$ Pa). Inset: Schematic of the ridge profile. (b) Width, λ (green circles), and amplitude, δ (blue squares), of the ridge for the same shell as in (a), as a function of the pressure load, Δp. The solid lines correspond to the integration of the *elastica* for the amplitude (respectively, width) accounting for the shell thickness [23]. (c) Linear dependence of λ with respect to the elastopneumatic length $\ell_{ep} = (B/\Delta p)^{1/3}$ for the PDMS shell ($R = 38.5$ mm, $195 < h\ [\mu$m$] < 450$, $G = 2.2$ mm). The solid line corresponds to our model when accounting for the effect of the shell thickness on λ.

in Fig. 3(b). As Δp increases, both λ and δ decrease, such that the aspect ratio δ/λ increases and the ridges become sharper.

The evolution of the shape of the ridges with Δp is rationalized by further reducing the problem to a two-dimensional construct that considers a slice of the shell perpendicular to the ridge, and modeling it as an *elastica* with bending stiffness $B = Eh^3/12(1 - \nu^2)$ [23]. In Fig. 3(a), we present a family of solutions for loadings in the range $0 \leqslant \Delta p\ [\text{kPa}] \leqslant 101$, for the shell considered above. For relatively low values of Δp, the solution has a sinusoidal profile [Fig. 3(a), blue curves], similarly to a ruck on a rug [40], whereas at high Δp [Fig. 3(a), red curves], the ridges collapse onto the surface of the mandrel and become sharper. In Fig. 3(a), we superpose the computed shape, for the specific case of $\Delta p = 510$ Pa, on top of the experimental profile (dotted line). Favorable quantitative agreement is found with no adjustable parameters.

Likewise, the evolution of the amplitude, δ, and width, λ, of the ridge, as a function of Δp is well captured by our reduced *elastica* description while taking the finite shell thickness into account [23] [Fig. 3(b)]. Note that, in this regime, the shell is almost entirely in contact with the mandrel. Surprisingly, even if our reduced model neglects the initial stretching in the ridges, it does successfully capture the evolution of both the profile and dimensions of the ridges, as a function of Δp. However, our description is limited to the central part of the ridges and fails to describe the interconnection of the network, where stretching is likely localized. In Fig. 3(c), we plot λ versus $\ell_{ep} = (B/\Delta p)^{1/3}$, the *elastopneumatic length* set by the balance of elasticity of the shell and the pressure loading, for three

shells of thickness $h = \{195, 240, 450\}\ \mu$m, $R = 38.5$ mm. and $G = 2.2$ mm. All the data collapse onto a master curve with $\lambda \sim \ell_{ep}$. Integration of the model yields the solid lines in Fig. 3(c) when accounting for the finite shell thickness [23]. At high values of Δp, the theory suggests that there is a lower bound at $\ell_{ep} \approx 1$, below which self-contact in the ridge occurs and the description is no longer valid. This is consistent with our observation that the experimental data in Fig. 3(c) departs from the $\lambda \sim \ell_{ep}$ regime when $\ell_{ep} \simeq 1$. In physical units, we find that $\lambda \sim \Delta p^{-1/3}$ such that producing sharp ridges requires relatively high pressures (considerably larger than the atmospheric pressure). In turn, we observe that the variation of δ with Δp is weaker than that of λ [see Fig. 3(b)]. Consequently, the sharpness (aspect ratio) of the ridge, δ/λ, can be readily varied and controlled through Δp, a single scalar parameter.

The ability to control dimpled patterns on demand could find applications for the fabrication of microlens arrays [41,42], nanoscale surface patterning [6], or tunable aerodynamic drag reduction [18]. Our study may also extend avenues for geometry-dominated responses in the buckling of shells that have been recently developed at the microscale, such as colloids that self-assemble [13], Janus-like particles with regions of distinct surface topography [32], or deformation of colloidosomes [15].

ACKNOWLEDGMENT

[1] R. F. Shepherd, F. Ilievski, W. Choi, S. A. Morin, A. A. Stokes, A. D. Mazzeo, X. Chen, M. Wang, and G. M. Whitesides, Proc. Natl. Acad. Sci. USA **108**, 20400 (2011).

[2] E. Brown, N. Rodenberg, J. Amend, A. Mozeika, E. Steltz, M. R. Zakin, H. Lipson, and H. M. Jaeger, Proc. Natl. Acad. Sci. USA **107**, 18809 (2010).

[3] J. Shim, C. Perdigou, E. R. Chen, K. Bertoldi, and P. M. Reis, Proc. Natl. Acad. Sci. USA **109**, 5978 (2012).

[4] J. L. Silverberg, J.-H. Na, A. A. Evans, B. Liu, T. C. Hull, C. D. Santangelo, R. J. Lang, R. C. Hayward, and I. Cohen, Nat. Mater. **14**, 389 (2015).

[5] N. P. Bende, A. A. Evans, S. Innes-Gold, L. A. Marin, I. Cohen, R. C. Hayward, and C. D. Santangelo, Proc. Natl. Acad. Sci. USA **112**, 11175 (2015).

[6] N. Bowden, S. Brittain, A. G. Evans, J. W. Hutchinson, and G. M. Whitesides, Nature (London) **393**, 146 (1998).

[7] B. Li, F. Jia, Y.-P. Cao, X.-Q. Feng, and H. Gao, Phys. Rev. Lett. **106**, 234301 (2011).

[8] A. S. Gladman, E. A. Matsumoto, R. G. Nuzzo, L. Mahadevan, and J. A. Lewis, Nat. Mater. **15**, 413 (2016).

[9] P. M. Reis, J. Appl. Mech. **82**, 111001 (2015).

[10] B. Florijn, C. Coulais, and M. v. Hecke, Phys. Rev. Lett. **113**, 175503 (2014).

[11] M. Schenk and S. D. Guest, Proc. Natl. Acad. Sci. USA **110**, 3276 (2013).

[12] E. Katifori, S. Alben, E. Cerda, D. R. Nelson, and J. Dumais, Proc. Natl. Acad. Sci. USA **107**, 7635 (2010).

[13] S. Sacanna, W. T. M. Irvine, P. M. Chaikin, and D. J. Pine, Nature (London) **464**, 575 (2010).

[14] J. Lidmar, L. Mirny, and D. R. Nelson, Phys. Rev. E **68**, 051910 (2003).

[15] A. D. Dinsmore, M. F. Hsu, M. Nikolaides, M. Marquez, A. Bausch, and D. Weitz, Science **298**, 1006 (2002).

[16] R. L. Carlson, R. L. Sendelbeck, and N. J. Hoff, Exp. Mech. **7**, 281 (1967).

[17] S. Adriaenssens, P. Block, D. Veenendaal, and C. Williams, *Shell Structures for Architecture: Form Finding and Optimization* (Routledge, Abingdon/New York, 2014).

[18] D. Terwagne, M. Brojan, and P. M. Reis, Adv. Mater. **26**, 6608 (2014).

[19] Y. P. Cao, B. Li, and X. Q. Feng, Soft Matter **8**, 556 (2012).

[20] D. Breid and A. J. Crosby, Soft Matter **9**, 3624 (2013).

[21] N. Stoop, R. Lagrange, D. Terwagne, P. M. Reis, and J. Dunkel, Nat. Mater. **14**, 337 (2015).

[22] A. Lee, P.-T. Brun, J. Marthelot, G. Balestra, F. Gallaire, and P. M. Reis, Nat. Commun. **7**, 11155 (2016).

[23] See Supplemental Material at http://link.aps.org/supplemental/10.1103/PhysRevMaterials.1.025601 for details on the methods and a movie of the periodic buckling patterns.

[24] B. Audoly and Y. Pomeau, *Elasticity and Geometry: From Hair Curls to the Non-Linear Response of Shells* (Oxford University Press, Oxford, 2010).

[25] M. Gomez, D. E. Moulton, and D. Vella, Proc. R. Soc. A **472**, 20150732 (2016).

[26] J. W. Hutchinson, J. Appl. Mech. **34**, 49 (1967).

[27] J. Paulose and D. R. Nelson, Soft Matter **9**, 8227 (2013).

[28] J. W. Hutchinson, Proc. R. Soc. A **472**, 20160577 (2016).

[29] L. Pauchard and S. Rica, Philos. Mag. B **78**, 225 (1998).

[30] A. Nasto, A. Ajdari, A. Lazarus, A. Vaziri, and P. M. Reis, Soft Matter **9**, 6796 (2013).

[31] P.-G. de Gennes, Rev. Mod. Phys. **64**, 645 (1992).

[32] S. C. Glotzer and M. J. Solomon, Nat. Mater. **6**, 557 (2007).

[33] D. R. Nelson, Phys. Rev. B **28**, 5515 (1983).

[34] M. Brojan, D. Terwagne, R. Lagrange, and P. M. Reis, Proc. Natl. Acad. Sci. USA **112**, 14 (2015).

[35] F. López Jiménez, N. Stoop, R. Lagrange, J. Dunkel, and P. M. Reis, Phys. Rev. Lett. **116**, 104301 (2016).

[36] J. W. Hutchinson and W. T. Koiter, Appl. Mech. Rev. **23**, 1353 (1970).

[37] A. Lee, F. López Jiménez, J. Marthelot, J. W. Hutchinson, and P. M. Reis, J. Appl. Mech. **83**, 111005 (2016).

[38] F. López Jiménez, J. Marthelot, A. Lee, J. W. Hutchinson, and P. M. Reis, J. Appl. Mech. **84**, 034501 (2017).

[39] J. M. T. Thompson, Aeronaut. Quart. **13**, 189 (1962).

[40] D. Vella, A. Boudaoud, and M. Adda-Bedia, Phys. Rev. Lett. **103**, 174301 (2009).

[41] E. P. Chan and A. J. Crosby, Adv. Mater. **18**, 3238 (2006).

[42] I. Jung, J. Xiao, V. Malyarchuk, C. Lu, M. Li, Z. Liu, J. Yoon, Y. Huang, and J. A. Rogers, Proc. Natl. Acad. Sci. USA **108**, 1788 (2011).